RSC Advances

ROYAL SOCIETY OF CHEMISTRY

www.rsc.org/advances

Effect of Strontium deficiency on the Structural, Magnetic and Magnetocaloric properties of $La_{0.65}Eu_{0.05}Sr_{0.3-x}MnO_3$ ($0 \leq x \leq 0.15$) perovskites

Ridha Bellouz [a*], Marwène Oumezzine [a], Aziz Dinia [b], Guy Schmerber [b], El-Kebir Hlil [c], Mohamed Oumezzine [a]

[a] *Laboratoire de Physico-chimie des Matériaux, Département de Physique, Faculté des Sciences de Monastir, Université de Monastir, Monastir 5019, Tunisia.*

[b] *Institut de Physique et Chimie des Matériaux de Strasbourg (IPCMS) UMR 7504 CNRS-Université de Strasbourg, 23 rue du Lœss, B.P. 43, 67034 Strasbourg Cedex 2, France*

[c] *Institut Néel, CNRS–Université Joseph Fourier, B.P. 166, 38042 Grenoble, France.*

Abstract

We have investigated the effect of nominal strontium deficiency on the structure, magnetic and magnetocaloric properties of $La_{0.65}Eu_{0.05}Sr_{0.3-x}MnO_3$ (x=0, 0.10 and 0.15) perovskites. The nanocrystalline samples were prepared by sol-gel-based Pechini method. Rietveld refinement of the X-ray diffraction patterns, shows the formation of single-phase compositions with rhombohedral symmetry (space group R-3c, no. 167). Raman spectra at room temperature reveal gradual change in phonon modes with increasing nominal strontium deficiency. All samples undergo paramagnetic-ferromagnetic (PM-FM) transition. The Curie temperature decreases linearly with increasing x and changes from 355 K for x = 0 to 280 K for x = 0.15. Arrott plot analyses and a universal curve method were applied for studying the order of the magnetic transition in this system, found to be of second order. As strontium deficiency content increased further, peak entropy values were seen to decline. However, a simultaneous broadening of the $\Delta S_M^{\max}$ peaks led to enhanced relative cooling power (RCP) in the Sr-deficiency samples of up to 22% over that of $La_{0.65}Eu_{0.05}Sr_{0.3}MnO_3$. $La_{0.65}Eu_{0.05}Sr_{0.15}MnO_3$ exhibits the largest RCP value of 283 $J.kg^{-1}$ at 280 K among the compounds investigated up to 5 T applied field. Through these results, $La_{0.65}Eu_{0.05}Sr_{0.3-x}MnO_3$ materials are strongly suggested for the use as active refrigerants for magnetic refrigeration technology near and above room temperature.

Keywords: Magnetocaloric effect, Magnetic properties, Pechini sol–gel method, X-ray diffraction.

1. Introduction

The perovskite manganites of $R_{1-x}A_xMnO_3$ (where R and A are trivalent rare earth and divalent alkaline earth ions, respectively) have been the subject of significant research interest because of the intriguing underlying physics showing marked colossal magnetoresistance (CMR) and magnetocaloric effects (MCE). From the applications perspective, interest in these materials arose initially from their potential applications in hard disks, magnetic sensors, spin-electronic devices, and magnetic refrigerants.[1-4]

The close relation between electrical transport and magnetism in these materials has been explained by many theories, such as double-exchange (DE) interaction,[5] Jahn–Teller effect,[6] and phase separation.[7] In these manganite materials, the doping of the rare-earth results in a mixed Mn^{3+}/Mn^{4+} valence and introduces mobile electrons leading to a quasi-metallic conductivity and the ferromagnetic ground state. Hence, the presence of mixed valence states of Mn ions in the doped manganites gives rise to the competing double exchange (DE) and super-exchange (SE) interactions.[8,9] It modifies the Mn^{3+}– O^{2-}– Mn^{4+} network and in turn largely affects their magnetotransport properties as well as MCE.[10-13]

The manganites have additional advantages such as low cost, good chemical stability, easy preparation and more importantly the ability to tailor their magnetic transition temperatures close to room temperature by R-site or Mn-site substitution. One recent example of this chemical substitution for tuning T_C in manganites is in the $La_{0.7}Sr_{0.3}MnO_3$ (LSMO) system, which is a colossal magnetoresistive ferromagnetic manganite with T_c~370 K, and either by substitution of the La ion by the rare-earths Nd,[14] Pr,[15] Eu,[16] or by substitution of Mn ions by other transition metal ions such as Cr, Fe, Zn, Ti, etc.[17-20] On the other hand, the ceramic preparation route, such as the conventional solid-state reaction method, the sol–gel method and combustion thermal spray techniques were used to prepare rare-earth perovskite materials. The method of synthesis plays an important role on the quality and the

magnetocaloric properties of materials.[21] However, only few studies have been proposed to discuss the deficiency effect in manganites system. Deficiency in this system is recognized to lead to a change of Mn^{3+}/Mn^{4+} ratio, thus, which can change the physical properties in manganites.[22-25]

In this paper, we report on the structure, magnetic and magnetocaloric properties of Sr deficient $La_{0.65}Eu_{0.05}Sr_{0.3-x}MnO_3$ manganite prepared by the sol-gel-based Pechini method. The experimental results reveal that the Curie temperature is adjusted to near room temperature and this is accompanied by an enhancement of the maximum magnetic entropy change. The phenomenological universal curve of the field dependence of the magnetic entropy ΔS_M has been used to study the nature of magnetic phase transition in our materials.

2. Experimental details

Polycrystalline samples of $La_{0.65}Eu_{0.05}Sr_{0.3-x}MnO_3$ were prepared using the Pechini sol-gel method and a mixture of oxides and precursors, $La(NO_3)_3.6H_2O$ (Sigma-Aldrich, 99%), $Sr(NO_3)_2$ (Sigma-Aldrich, 99.99%), $Eu(NO_3)_3.5H_2O$ (Sigma-Aldrich, 99.9%) and Mn_2O_3 (Sigma-Aldrich, 99%). This method consisted in the preparation of metal nitrates that were added to a solution of citric acid (CA) (Sigma-Aldrich, 99%) and ethylene glycol (EG) (Sigma-Aldrich, ≥ 99%) to form a polymeric resin. However, the initial solution was prepared by mixing distilled water and the nitrates (properly weighed according to the specific composition), CA and EG. The resulting solution was heated by constant stirring at temperatures of 80 °C. After evaporation of water at 80 -100 °C, the viscosity of the solution increases and further heating leads to the formation of polymeric resin.

The resin was pre-calcined (673 K for 3 h) to eliminate the organic material, ground and calcined again (973 K for 15 h) to eliminate the residual organic material. The obtained black powder was cold-pressed into pellets with diameter 13 mm and thickness of about 2-3 mm under a pressure of 5 Tons/cm^2. After that, the powder was sintered at 1273 K for 12 hours in

air. The morphological properties of the samples were investigated by scanning electron microscopy (SEM) using a JSM-6400 apparatus working at 20 kV. Energy dispersive X-ray analysis (EDAX) has been performed to determine the composition of the samples. The Mn^{4+}/Mn^{3+} ratios as well as the oxygen content of the samples were determined by iodometric titration. Typically, about 100 mg of the sample was dissolved in 10 ml of 1:10 HCl containing about 1 g of solid KI. Liberated iodine was titrated against standard sodium thiosulfate (0.04 N) solution using starch as an indicator. The structural characterization was done through X-ray diffraction patterns (XRD) using a "Panalytical X'pert Pro" diffractometer with CuK_α radiation (λ=1.5406Å). Raman spectra were collected at room temperature (300 K) with a Horiba LabRAM micro-Raman spectrometer (model HR 800). We have used one incident light of 632.8 nm focused on the sample with a ×50 microscope objective. Typical power densities on the samples' surface were not higher than 0.9 $mW/\mu m^2$ in order to avoid over-heating and damaging of the powders. Five spectra were at least recorded on different zones for the same sample. Magnetic measurements were performed using a BS2 magnetometer at Louis Néel Laboratory at Grenoble, where we measured the magnetization versus applied magnetic field in a temperature range near T_C.

3. Results and Discussion

3.1. Structural properties

Fig. 1.(a) shows the XRD patterns of $La_{0.65}Eu_{0.05}Sr_{0.3-x}MnO_3$ ($0 \leq x \leq 0.15$) powders. The diffraction peaks are narrow and intense in all XRD patterns, indicating that the studied samples are well crystallized. No impurity peaks are found within the experimental error. All diffraction peaks can be indexed in the rhombohedral distorted perovskite structure (space group R-3c), in which the (La, Eu, Sr) atoms are at 6a (0, 0, 1/4) positions, Mn at 6b (0, 0, 0) and O at 18e (x, 0, 1/4). The structural parameters were determined by Rietveld refinement method. The data were first analyzed with a "whole pattern fitting" algorithm in order to

determine accurately the profile shape function, background and the cell parameters. A typical example of the Rietveld refinement to the XRD data for $La_{0.65}Eu_{0.05}Sr_{0.2}MnO_3$ nanopowder is shown in **Fig. 1.(b)**. Detailed results of Rietveld refinement are listed in **Table 1**, where a and c are the hexagonal cell parameters, V is the unit cell volume, B_{iso} is the isotropic thermal parameter and x is the oxygen position. The residuals for the weighted patterns R_{wp}, the pattern R_p, the structure factor R_F and the goodness of fit χ^2 are also reported in this table. The residuals for the weighted pattern R_{wp}(%) and the goodness of fit χ^2 across the compositional series resulted below 3% and below 2%, respectively. One can see from **Table 1** that the lattice parameters a, c and the volume V increase when $\langle r_A \rangle$ decreases. The presence of a strontium deficiency in our samples induces an increase of the Mn^{4+}content. Since the average ionic radius of Mn^{4+} (0.53 Å) is smaller than that of Mn^{3+} (0.65 Å), [26] the increase of the unit cell volume with strontium-vacancies cannot be explained in terms of Mn^{4+} amount. It may rather be related to an average ionic radius $\langle r_A \rangle$ of the A cation site with a vacancy radius $\langle r_V \rangle$ larger than the radius of the Sr^{2+} cation.[22] The Mn-O bond length and the Mn-O-Mn bond angles obtained from the Rietveld refinement are presented in **Table 1**. From the results of the average distances of Mn–O and the average angles of Mn–O–Mn, it is considered that each MnO_6 octahedron has little distortion. These observations are consistent with the value of the Goldschmid tolerance factor t, defined as:

$$t = \frac{< r_A > + r_O}{\sqrt{2}(< r_B + r_O)} \qquad (1)$$

where r_A, r_B and r_O are respectively the average ionic radii of A and B perovskite sites and of the oxygen anions. The tolerance factor is an important structural parameter, which reflects the local microscopic distortion from the ideal perovskite (ABO_3) structure (t = 1), for which the B–O–B bond angle θ is equal to 180°.

The surface morphology of the samples $La_{0.65}Eu_{0.05}Sr_{0.3-x}MnO_3$ ($0 \leq x \leq 0.15$) has been investigated using SEM. **Fig. 2** presents the SEM micrographs of the sintered pellets and shows that the samples are constituted of strongly connected large grains, forming almost homogenous particles. The average crystallites sizes, determined by Rietveld refinement,[19] are estimated to be between 84 and 97 nm (+/- 2 nm). These values are close to those shown by SEM micrographs (the average particles size is ~100 +/- 10 nm). To analyse the composition of $La_{0.65}Eu_{0.05}Sr_{0.3-x}MnO_3$ ($0 \leq x \leq 0.15$) samples, energy dispersive X-ray analysis (EDAX) was used. The spectra illustrated in **Fig. 3** show the elemental distribution in the samples. The results demonstrated that there is no unwanted element in the samples. This implies that the samples are not contaminated during the synthesis process. The results of the analysis are largely summarized in **Table 2.** If it is assumed that, La, Eu and Sr are present in all the samples in their respective stoichiometric ratio and Mn is present in a mixed valence state (Mn^{3+} and Mn^{4+}), then the chemical formula of the compounds can be written as: $La^{3+}_{0.65}Eu^{3+}_{0.05}Sr^{2+}_{0.3-x}Mn^{3+}_{1-\Delta}Mn^{4+}_{\Delta}O_y$ (x= 0, 0.10 and 0.15). The value of Δ of the samples was determined by iodometric titration method.[27] The average error of the Mn^{4+}/ Mn^{3+} ratio determination by iodometric was found to be ± 0.03. The oxygen content, y, was calculated from the equation, $y = \frac{5.7 + \Delta}{2} - x$. It is noticed that the Mn^{4+}/ Mn^{3+} ratio increases with increasing the strontium deficiency while the oxygen content is close to stoichiometry. We must mention that the oxygen stoichiometry is purely based on the mixed oxidation state of Mn and hence the amount of the strontium vacancies. The calculated values of the Mn^{4+}/ Mn^{3+} ratio (these values are average of many titrations) and oxygen content y are illustrated in **Table 1**.

3.2. Raman spectroscopy

Raman scattering is a powerful tool for the characterization of material and is a qualitative probe of the presence of lattice defect in solids, such as structure transition, lattice distortion,

cation distribution and magnetic ordering. The ideal cubic ABO_3 perovskite structure does not possess Raman active phonons since all the five atoms of the unit cell occupy centrosymmetrical sites. The (i) mismatch of the ionic radii of the ions in the unit cell and the (ii) J–T effect associated with the Mn^{3+} ions give origin to the orthorhombic (Pnma) and the rhombohedral (R-3c) structures, both of them presenting Raman active phonons. According to the group theory, for R-3c (D_{3d}^6) rhombohedral structure, thirty vibrational degrees of freedom at the Γ point are distributed among the irreducible representation as:

$\Gamma(D_{3d}^6) = 2A_{1u} + 3A_{2g} + A_{1g} + 4A_{2u} + 4E_g + 6E_u$

where only five (A_{1g}+$4E_g$) modes are Raman active, ($3A_{2u}$ + $4E_u$) are IR active modes and the remaining $2A_{1u}$ + $3A_{2g}$ are silent modes. The classifications of Raman active modes are $1A_{1g}$ + $1E_g$ as rotational or tilt modes; $1E_g$ bending and $1E_g$ antistretching of the MnO_6 octahedra and the remaining E_g is related to a vibration of A ions.[28,29]

The Raman spectra of $La_{0.65}Eu_{0.05}Sr_{0.3-x}MnO_3$ (x = 0, 0.10, 0.15) samples at room temperature in the frequency range of 200–900 cm^{-1} is shown in **Fig. 4**. The spectrum presents four peaks located at 310 (A_{1g}), 369 (E_g) 495 (E_g) and 650 (E_g) cm^{-1}. These peaks are associated with rotational-, bending-, and stretching-like vibrations of the MnO_6 octahedra, respectively. In the present measurement the absence of one E_g mode might be due to disorder produced in the sample because of the shift in position or vacancies of the atoms around the oxygen atoms or change of the Mn valence. It has been noticed from the graph that with increasing strontium-vacancy x, the Raman scattering intensity of the phonon modes are increasing. It is thus noticed that all the E_g vibrational modes shift slightly towards high wave number side, the shift of the wavenumber may be due to the change in the Mn–O distance.[30]

3.3. Magnetic properties

In order to study the strontium-vacancies effect on the magnetic properties, magnetization (M) versus temperature (T) under an applied magnetic field of 500 Oe for $La_{0.65}Eu_{0.05}Sr_{0.3-x}MnO_3$

(x = 0, 0.10 and 0.15) is measured and reported in **Fig. 5.** The curves reveal paramagnetic (PM) to ferromagnetic (FM) phase transition, corresponding to the Curie temperature T_C. The ferromagnetic ordering transition temperatures T_C, defined as the one corresponding to the peak of dM/dT (inset, **Fig. 5**), are summarized in **Table 1.**

The introduction of the strontium vacancies in our samples involves a partial conversion of Mn^{3+} to Mn^{4+} ions according to the formula $La^{3+}_{0.65}Eu^{3+}_{0.05}Sr^{2+}_{0.3-x}Mn^{3+}_{0.7-2x}Mn^{4+}_{0.3+2x}O_3$. The increase of the strontium vacancies content x leads to an increase of Mn^{4+} ion number which produces a decrease in the DE interaction (Mn^{3+}- O^{2-}- Mn^{4+}) and favors the SE interaction (Mn^{4+}- O^{2-}- Mn^{4+}) and as consequence a decrease of the Curie temperature T_C. The value of Mn^{4+}/Mn^{3+} ratio with increasing x obtained from iodometric titrations supports this argument (see **Table 1**). Based on the model of double exchange (DE), a lower T_C corresponds to a poorer overlap between Mn_{3d} and O_{2p} orbitals, resulting in a reduced bandwidth (W).[31] The bandwidth can be described empirically by $W \propto \cos w/(d_{Mn\text{-}O})^{3.5}$, where $w = (1/2(\pi - \theta_{Mn\text{-}O\text{-}Mn}))$ and d_{Mn-O} is the Mn–O bond length. Estimated values of the bandwidth W are given in **Table 1**.

In order to investigate the magnetic behavior at low temperatures, we have carried out magnetization measurements versus magnetic applied field up to 5 T at several temperatures (isothermal magnetization). These magnetization curves are reported in **Fig. 6** for (a) x=0, and (b) x=0.10 samples. The magnetization has been found to increase with decreasing temperature in the selected temperature range, where thermal fluctuation of spins decreases with decreasing temperature.

To determine the nature of the magnetic phase transition (first or second order) for our samples, we presented in **Figs. 7 (a, b)** the Arrott plot,[32] ($\mu_0 H/M$ versus M^2) for x=0 and x=0.10. All of the M^2 vs $\mu_0 H/M$ curves show positive slopes without inflection points, which is characteristic of second order transitions according to the Banerjee criterion.[33]

3.4. Magnetocaloric effect

MCE is an intrinsic property of magnetic materials. It is the response of the material toward the application or removal of a magnetic field. This response is maximized when the material is near its magnetic ordering temperature. Using the thermodynamic theory, the magnetic entropy change ΔS_M, which results from spin ordering and which is induced by the variation $\mu_0\Delta H$ of the magnetic applied field from 0 to $\mu_0 H$, is given by the following relation:,[34,35]

$$\Delta S_M = \mu_0 \int_0^H \left(\frac{\partial M(H,T)}{\partial T} \right)_H dH \qquad (2)$$

Experimentally, the magnetic entropy change ΔS_M is often evaluated by some numerical approximation methods. One is to use directly the measurements of M-T curve under different applied magnetic fields. In the case of small discrete field intervals, ΔS_M can be obtained approximately from Eq. (1) and written as:

$$\Delta S_M = \sum_i \left[\left(\frac{\partial M}{\partial T} \right)_{H_i} + \left(\frac{\partial M}{\partial T} \right)_{H_{i+1}} \right] \times \frac{\mu_0 \Delta H_i}{2} \qquad (3)$$

In the formula, $\left(\frac{\partial M}{\partial T} \right)_{H_i}$ is the experimental value obtained from M-T curve in magnetic field H_i. Another method is to use isothermal magnetization measurements. In the case of magnetization measurements at small discrete field and temperature intervals, ΔS_H can be expressed approximately from Eq. (2) as:

$$\Delta S_M = \sum_i \frac{M_i - M_{i+1}}{T_{i+1} - T_i} \mu_0 \Delta H_i \qquad (4)$$

where M_i and M_{i+1} are the experimental values of the magnetization at T_i and T_{i+1}, respectively, under an applied magnetic field $\mu_0 H_i$. In this paper, we adopt the latter to evaluate the entropy change associated with applied field variation.

The magnetic entropy change ΔS_M for $La_{0.65}Eu_{0.05}Sr_{0.3-x}MnO_3$ (x=0, 0.10 and 0.15) was calculated from equation (3) using the magnetization isotherms in the vicinity of the ordering

temperature T_C. **Fig. 8** shows the temperature dependence of magnetic entropy change ($-\Delta S_M$) at various intervals of magnetic field. The maximum value of ΔS_M is found to be around T_C and it increases with the increase of the ΔH variation of the applied magnetic field. As an important result, these curves reveal that all samples present a large magnetocaloric effect. This $\left|\Delta S_M^{max}\right|$ is found to be sensitive to the strontium deficiency. Indeed, under $\mu_0 H$=5 T, $\left|\Delta S_M^{max}\right|$ is equal to 5.44, 5.15, and 4.96 J. kg^{-1}. K^{-1} for the samples of x= 0, 0.10 and 0.15, respectively.

Another useful parameter, which quantifies the efficiency of a magnetocaloric material, is the relative cooling power (RCP). It is the heat transfer between the hot and the cold tanks during an ideal refrigeration cycle. It can be defined as:

$$RCP = -\Delta S_M^{max} \times \delta_{FWHM}, \quad (5)$$

where $\delta_{FWHM} = \Delta T$ is the full-width at half maximum peak and $-\Delta S_M^{max}$ is the maximum value of magnetic entropy change that occurs at Curie temperature.

The RCP estimated in the present set of $La_{0.65}Eu_{0.05}Sr_{0.3-x}MnO_3$ (x=0, 0.10 and 0.15) samples increases with x (see Table 3). The largest RCP values for x = 0.15 is about 69% of that of pure Gd, the prototype magnetic refrigerant material (RCP = 410 J. kg^{-1}).[36] For comparison, the maximum magnetic entropy change, the Curie temperature, and the relative magnetic cooling efficiency of several manganese perovskites,[37,38] which could be used for room temperature magnetic refrigerators are presented in **Table 3**. From these results, we can estimate that our materials are potential candidates to magnetic refrigeration applications.

As shown in the insets of **Fig. 8**, ΔS_M^{max} and RCP exhibit a linear rise with increasing field which indicates that a much larger entropy change and relative cooling power are to be expected at higher magnetic field, satisfying thereby the effects of spin-lattice coupling associated with changes in the magnetic ordering process in the samples.[39]

The phenomenological universal curve of the field dependence of the magnetic entropy ΔS_M proposed by Franco et al.[40,41] can be used as a further criterion to distinguish the order of the magnetic phase transition. This phenomenological universal curve can be constructed by normalizing all the ΔS_M (T) curves by their respective maximum ΔS_M^{max}, namely, $\Delta S' = \Delta S_M (T) / \Delta S_M^{max}$ rescaling the temperature axis below and above T_C as defined in Eq. (6) with an imposed constraint that the position of two additional reference points in the curve corresponding to $\theta \pm 1$.

The construction of the phenomenological universal curve requires to normalize each isofield ΔS_M (T) to its maximum value $\left|\Delta S_M^{max}\right|$ and then rescaling the temperature axis defining a new variable θ,[42]

$$\theta = -(T-T_C)/(T_{R1}-T_C) \quad \text{for} \quad T \le T_C,$$
$$\theta = (T-T_C)/(T_{R2}-T_C) \quad \text{for} \quad T > T_C \qquad (6)$$

Here, the reference temperatures T_{R1} and T_{R2} are chosen such that $\Delta S_M (T_{r1}) = \Delta S_M (T_{r2}) = \Delta S_M^{max}/2$. For the materials undergoing second-order phase, the rescaled magnetic entropy change curves follow an universal behavior. While the scaled ΔS_M curves do not collapse as a single curve, the materials undergo a first-order phase transition.[43]

The normalized entropy change curves as a function of the rescaled temperature for $La_{0.65}Eu_{0.05}Sr_{0.3-x}MnO_3$ (x = 0, 0.10 and 0.15) samples are plotted in **Fig. 9**. It can be obviously seen that the experimental data collapse into an universal curve for the studied samples. This behavior proves that the studied manganites undergo the second-order magnetic phase transition, which is consistent with the trends observed in the Arrott plots (**Fig. 7**). The universal curve can be well fitted by a Lorentz function such as:

$$\Delta S' = \frac{a}{b + (\theta - c)^2} \qquad (7)$$

where a, b, and c are the free parameters. By taking into account the asymmetry of the curve (see the inset of Fig. 7, for x = 0), two different sets of constants have to be used: for $T < T_C$, a = 1.14 ± 0.03, b = 1.03 ± 0.03 and c = 0.34 ± 0.05; and for $T > T_C$, a = 0.92 ± 0.05, b = 0.93 ± 0.04 and c = 0.025 ± 0.06.

In order to determine the field dependence of the experimental ΔS_M of the studied material, a local exponent is calculated using $\Delta S_M = a(\mu_0 H)^n$ as,[44]

$$n = \frac{d \ln \Delta S_M}{d \ln H} = -\frac{\mu_0 H}{\Delta S_M}\left(\frac{\partial M}{\partial H}\right)_H \qquad (8)$$

where a is a constant and the exponent *n* depend on the values of field and temperature. In a mean field approach, the value of *n* at the Curie temperature is predicted to be 2/3.[45]

Fig. 10 shows the dependence of the local exponent *n* for the studied samples for typical field changes up to 5 T. All the curves follow the universal behavior described by Franco et al.[41] At T_C, an increase in *n* is observed with the decrease in the field change. This can be associated to the nonsaturation of the sample. Thus, the local exponent n is close than 2/3 for small field changes. The n values around T_C are 0.65, 0.62, and 0.60 for x = 0, 0.10 and 0.15 respectively, which confirms the validity of the mean field model in the description of our samples near the transition temperature. These values are similar to those obtained for soft magnetic materials containing rare earth metals.[46] When plotting the so-called local n (T) exponents, one may see that the n (T) values are weakly affected by a magnetic field strength, as shown in the inset of **Fig. 10**. In general, an application of stronger magnetic field nonuniformly pulls the n (T) curves down by a few percent. The shift seems to be minimum in vicinity of Curie temperature and is enhanced both below and above T_C. For the ideal, single-phase and perfectly homogeneous materials the n(T) exponent is expected to be field independent at the Curie temperature.[47,48] However, serious deviations from this ideal model observed in various materials are ascribed to such factors, like secondary phases (negligible in

manganites studied) and imperfections, e.g., inside grain boundaries, which may broaden a distribution of Curie temperatures and in turn cause that the sample is not saturated in a whole volume, when a magnetic field is not strong enough.

Conclusion

We have studied the magnetic and magnetocaloric properties of $La_{0.65}Eu_{0.05}Sr_{0.3-x}MnO_3$ prepared using the Pechini sol–gel method. Rietveld refinement of XRD patterns shows that all compounds possess rhombohedral structure with R-3c space group. The increase of the strontium vacancies content x leads to an increase of Mn^{4+} ion number which produces a decrease in the double exchange interaction (Mn^{3+}- O^{2-}- Mn^{4+}) and favors the super-exchange interaction (Mn^{4+}- O^{2-}- Mn^{4+}), thus leading to decrease of the Curie temperature T_C. Magnetic measurements show that all compounds exhibit a FM–PM second order transition. A large MCE is observed near T_C. The maximum of the magnetic entropy change $\left|\Delta S_M^{\max}\right|$ in a magnetic field change of 5 T is found to be 5.44, 5.15 and 4.96 J. kg^{-1}. K^{-1} for x=0, 0.10 and 0.15, respectively. Broad operating temperature range along with moderate values of $\left|\Delta S_M^{\max}\right|$ and RCP make these compounds potential candidates for magnetic refrigeration applications. An uniform phenomenological function that describes the magnetic entropy change is found for these materials.

References

1 A. P. Ramirez, *J. Phys. Condens. Matter*., (1997), **9,** 8171.

2 Z. B. Guo, Y. W. Du, J. S. Zhu, H. Huang, W. P. Ding, and D. Feng, *Phys. Rev. Lett.,* (1997), **78,** 1142.

3 M. B. Salamon and M. Jaime, *Rev. Mod. Phys*., (2001), **73,** 583.

4 E. Dagotto, T. Hotta, A. Moreo, *Phys. Rep.***,** (2001), **344,** 1.

5 C. Zener, *Phys. Rev. B*, (1951), **82,** 403.

6 A. J. Millis*, Phys. Rev. B,* (1996), **53,** 8434.

7 S. Mori, C. H. Chen and S. W. Cheong, *Phys. Rev. Lett.*, (1998), **81,** 3972.

8 D. T. Morelli, A. M. Mance, J. V. Mantese, and A. L. Micheli, *J. Appl. Phys.,* (1996), **79,** 373.

9 L. E. Hueso, P. Sande, D. R. Miguéns, J. Rivas, F. Rivadulla and M. A. López-Quintela, *J. Appl. Phys.,* (2002), **91,** 729943.

10 B. Boy, A. Poddar and S. Das, *J. Appl. Phys.,* (2006), **100,** 104318.

11 J. J. Neumeier, K. Andres and K. J. McClellan, *Phys. Rev. B.,* (1999), **59,** 1701.

12 M. Muroi, R. Street and P. G. McCormik, *J. Appl. Phys.,* (2000), **87,** 3424.

13 J. Blasco, J. García, J. M. de Teresa, M. R. Ibarra, J. Perez, P. A. Algarabel, C. Marquina, and C. Ritter, *Phys. Rev. B.***,** (1997), **55,** 8905.

14 A. Hagaza, N. Kallel, S. Kallel, T. Guizouarn, O. Peña and M. Oumezzine, *J. Alloys Compd.***,** (2009), **486,** 250.

15 M. S. Anwar, F. Ahmed and B. H. Koo, *J. Alloys Compd.,* (2014), **617,** 893.

16 J. S. Amaral, M. S. Reis, V. S. Amaral, T. M. Mendonça, J. P. Araújo, P. B. Tavares and J. M. Vieira, *Mater. Sci. Forum.,* (2006), **299,** 514.

17 R. Bellouz, M. Oumezzine, E. K. Hlil and E. Dhahri, *J. Magn. Magn. Mater.,* (2015), **375**, 136.

18 M. Oumezzine, O. Peña, S. Kallel and M. Oumezzine, *J. Alloys Compd.,* (2012), **539,** 116.

19 Ma. Oumezzine, S. Zemni and O. Peña, *J. Alloys Compd.,* (2010), **508,** 292.

20 S. K. Barik, C. Krishnamoorthi and R. Mahendiran, *J. Magn. Magn. Mater.,* (2011), **323**, 1015.

21 W. A. Sun, J. Q. Li, W. Q. Ao, J. N. Tang and X. Z. Gong, *Powder Technol.,* (2006), **166,** 77.

22 M. Oumezzine, S. Kallel, O. Peña, N. Kallel, T. Guizouarn, F. Gouttefangeas and M. Oumezzine, *J. Alloys Compd.,* (2014), **582,** 640.

23 A. Ben Amor, M. Koubaa, W. Cheikhrouhou-Koubaa and A. Cheikhrouhou, *J. Alloys Compd.,* (2009), **467,** 78.

24 W. Cheikhrouhou Koubaa, M. Koubaa and A. Cheikhrouhou, *J. Alloys Compd.,* (2011), **509,** 4363.

25 W. Boujelben, A. Cheikh-Rouhou, J. Pierre and J. C. Joubert, *Physica B*., (2002), **321,** 37.

26 R. D. Shanon, *Acta Crystallogr. Sect. A Cryst. Phys. Diffr. Theor. Gen. Crystallogr*., (1976), **32,** 751.

27 J. Spooren, R. I. Walton and F. Millange, *J. Mater. Chem.,* (2005), **15,** 1542.

28 L. M. Carrón, A. de Andrés, M. J. Martínez-Lope, M. T. Casais and J. A. Alonso, *Phys. Rev. B.,* (2002), **66**,174303.

29 V. B. Podobedov, D. B. Romero, A. Weber, J. P. Rice, R. Schreekala, M. Rajeswari, R. Ramesh, T. Venkatesan and H. D. Drew, *Appl. Phys. Lett.*, (1998),**73,** 3217.

30 N. V. Minh and I. S. Yang. *Vibratio. Spectr.,* (2006), **42,** 353.

31 P. G. Radaelli, G. Iannone, M. Marezio, H. Y. Hwang, S. W. Cheong, J. D. Jorgensen and D. N. Argyriou, *Phys. Rev. B*., (1997), **56,** 8265.

32 L. M. R. Martinez and J. P. Attfield, *Phys. Rev. B.,* (1996), **54,** 5622.

33 B. K. Banerjee, *Phys. Lett.,* (1964), **12,** 16.

34 V. K. Pecharsky and K. A. Gschneidner Jr. *J. Magn. Magn. Mater.,* (1999), **200,** 44.

35 J. S. Amaral and V. S. Amaral, *J. Magn. Magn. Mater.,* (2010), **322,** 1552.

36 M. Földeàki, R. Chahine and T. K. Bose, *J. Appl. Phys.,* (1995), **77,** 3528.

37 K. A. Gschneidner Jr, V. K. Pecharsky, A. O. Tsokol, *Rep. Prog. Phys.*, (2005), **68,** 1479.

38 J. S. Amaral, M. S. Reis,V. S. Amaral, T. M. Mendonça, J. P. Araújo, P. B. Tavares and J. M. Vieira, *Mater. Sci. Forum*., (2006), **299,** 514.

39 S. Zemni, M. Baazaoui, Ja. Dhahri, H. Vincent and M. Oumezzine, *Materials Letters.,* (2009), **63,** 489.

40 V. Franco and A. Conde, Int. J. Refrigerat., (2010), **33,** 465.

41 V. Franco, R. C. Flores, A. Conde, Q. Y. Dong and H. W. Zhang, *J. Magn. Magn. Mater.***,** (2009), **321,** 1115.

42 V. Franco, J. S. Blázquez and A. Conde, Appl. Phys. Lett. **89** (2006) 222512.

43 C. M. Bonilla, J. H. Albillos, F. Bartolomé, L. M. García, M. P. Borderías, and V. Franco, *Phy. Rev. B.,* (2010), **81,** 224424.

44 T. D. Shen, R. B. Schwarz, J. Y. Coulter and J. D. Thompson, *J. Appl. Phys.,* (2002), **91,** 5240.

45 H. Oesterreicher and F. T. Parker, *J. Appl. Phys.*, (1984), **55,** 4334.

46 P. Nisha, S. S. Pillai, M. R. Varma and K. G. Suresh, *Solid State Sci.,* 2012, **14**, 40e47.

47 R. C. Flores, V. Franco, A. Conde, Q. Y. Dong and H. W. Zhang, *J. Magn. Magn. Mater.,* (2010), **322,** 804.

48 Q. Y. Dong, H. W. Zhang, J. R. Sun, B. G. Shen, and V. Franco, *J. App. Phy***.,** (2008), **103**, 116101.

Figure captions:

Fig. 1: (a) X-ray diffraction patterns of $La_{0.65}Eu_{0.05}Sr_{0.3-x}MnO_3$ ($0 \leq x \leq 0.15$) compounds at room temperature. **(b).** Rietveld refinement profile for x=0.10 performed using FULLPROF. Open circles correspond to experimental data and the lines are fits. Vertical bars represent the Bragg reflections for the space group R-3c. The difference pattern between the observed data and fits is shown at the bottom.The inset shows a zoom in the region between 2θ 34–64°

Fig. 2: SEM micrographs for $La_{0.65}Eu_{0.05}Sr_{0.3-x}MnO_3$ (x=0, 0.10 and 0.15) samples.

Fig. 3: EDAX images for $La_{0.65}Eu_{0.05}Sr_{0.3-x}MnO_3$ (x=0, 0.10 and 0.15) compositions.

Fig. 4: Raman spectrum of $La_{0.65}Eu_{0.05}Sr_{0.3-x}MnO_3$ (x=0, 0.10 and 0.15).

Fig. 5: Temperature dependence of magnetization for $La_{0.65}Eu_{0.05}Sr_{0.3-x}MnO_3$ (x=0, 0.10 and 0.15). The inset indicates the plot of dM/dT curve for determining T_C.

Fig. 6: Isothermal magnetization versus magnetic field around T_C of $La_{0.65}Eu_{0.05}Sr_{0.3-x}MnO_3$, (a) for x =0 and (b) for x = 0.10.

Fig. 7: Arrott plot of $\mu_0 H/M$ vs M^2 at different temperatures for $La_{0.65}Eu_{0.05}Sr_{0.3-x}MnO_3$, (a) x =0 and (b) x = 0.10.

Fig. 8: The temperature dependence of the magnetic entropy change (ΔS_M) under different applied magnetic fields and the inset represent (ΔS_M^{max}), and the relative cooling power (RCP) values versus applied magnetic field: (a) for x=0, (b) for x=0.10 and (c) for x=0.15.

Fig. 9: Normalized ΔS_M versus rescaled temperature θ for $La_{0.65}Eu_{0.05}Sr_{0.3-x}MnO_3$, the inset shows collapse of the experimental data onto the average curve and the solid line is the fit to Eq. (7).

Fig. 10: θ dependence of the local exponent n for $La_{0.65}Eu_{0.05}Sr_{0.3-x}MnO_3$ (x =0 and x = 0.10) for typical field changes. Inset shows the temperature variation of local n exponent calculated at typical magnetic fields.

Table captions:

Table 1: Detailed results of Rietveld refinement of $La_{0.65}Eu_{0.05}Sr_{0.3-x}MnO_3$ (x=0, 0.10 and 0.15) samples at room temperature.

Table 2: Results of EDAX analysis.

Table 3: Maximum entropy change $\left|\Delta S_M^{Max}\right|$ and relative cooling power (RCP), for $La_{0.65}Eu_{0.05}Sr_{0.3-x}MnO_3$ (x=0, 0.10, and 0.15), occurring at the Curie temperature (T_C) and under magnetic field variations, ΔH=1T or ΔH=5T, compared to several materials considered for magnetic refrigeration.

Figure captions:

Fig 1:

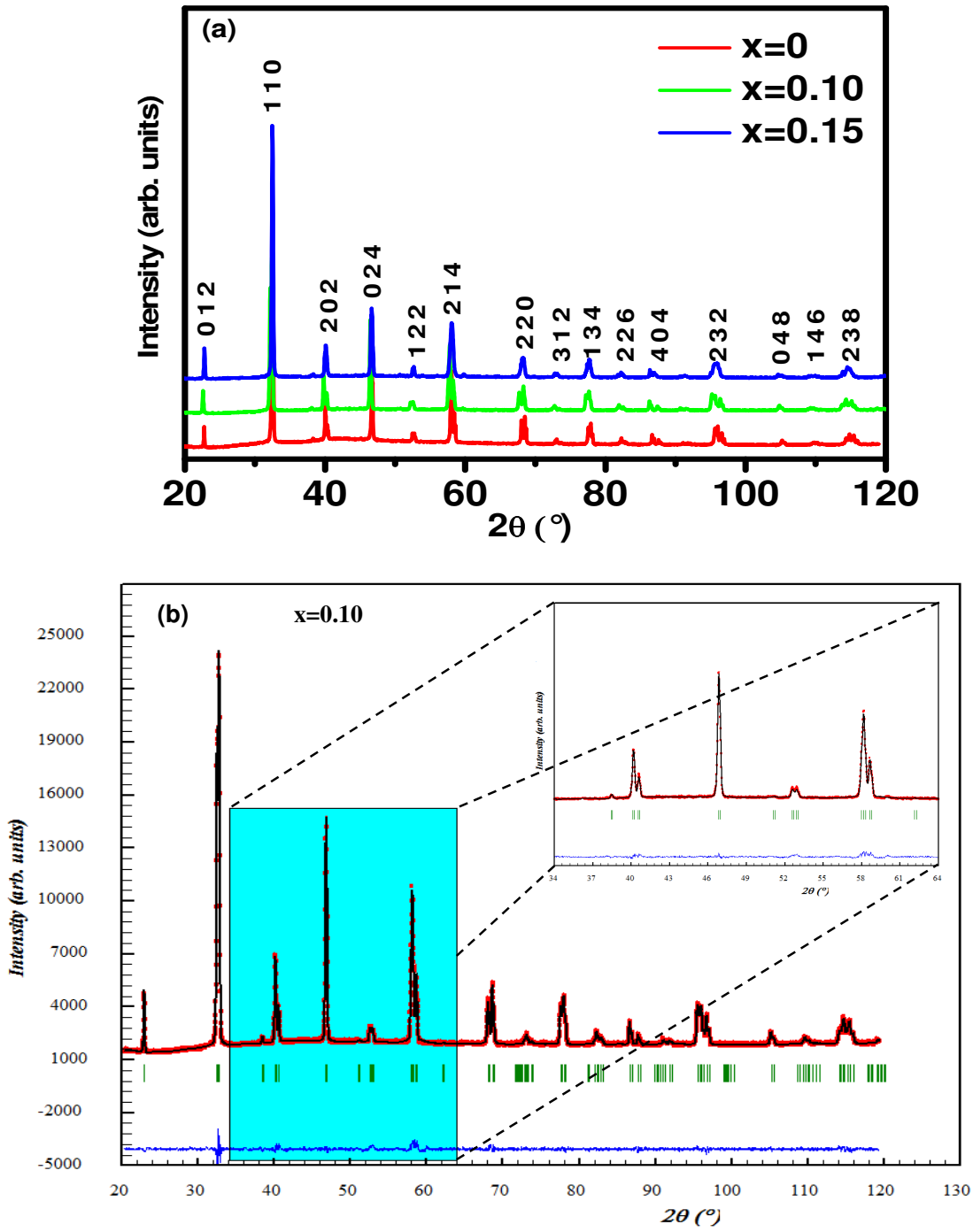

Fig 2:

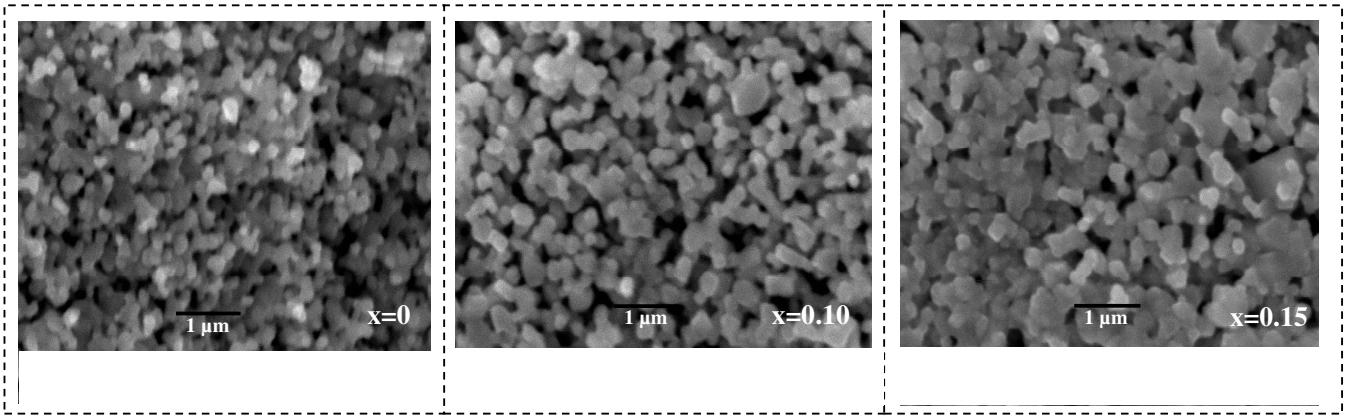

Fig 3:

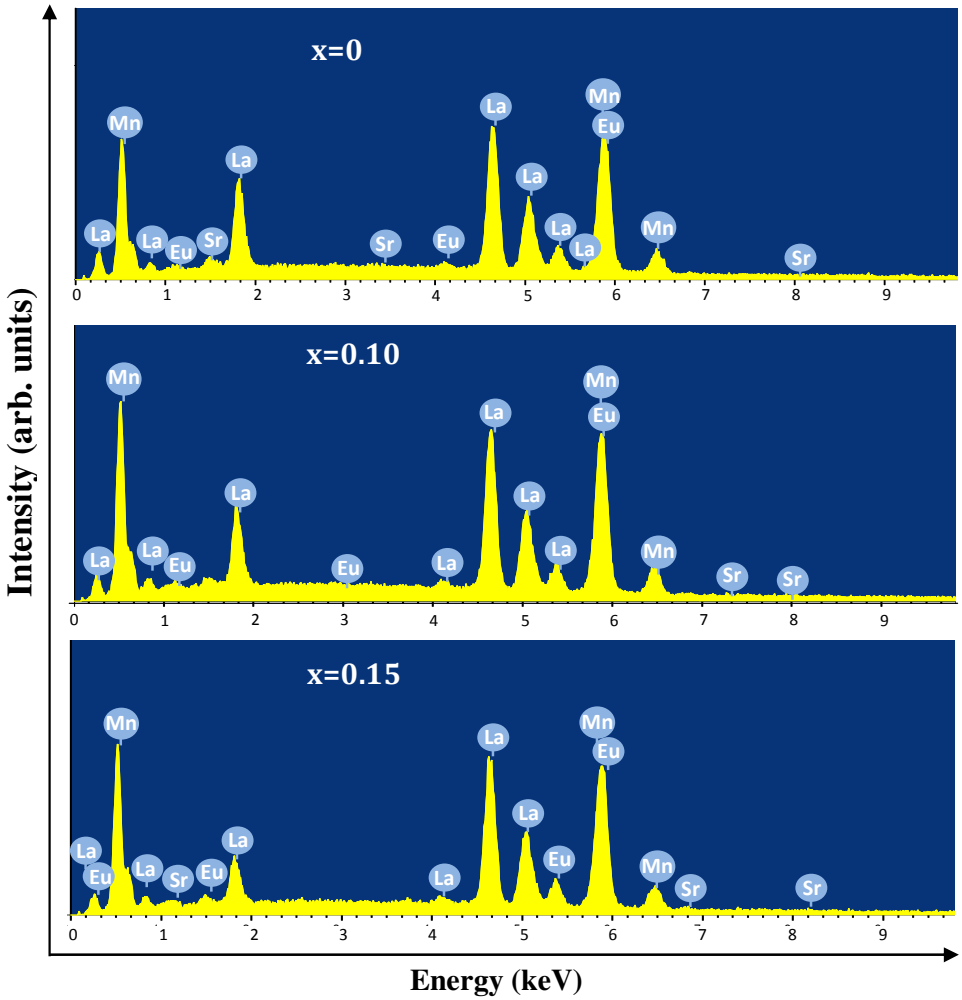

Fig. 4:

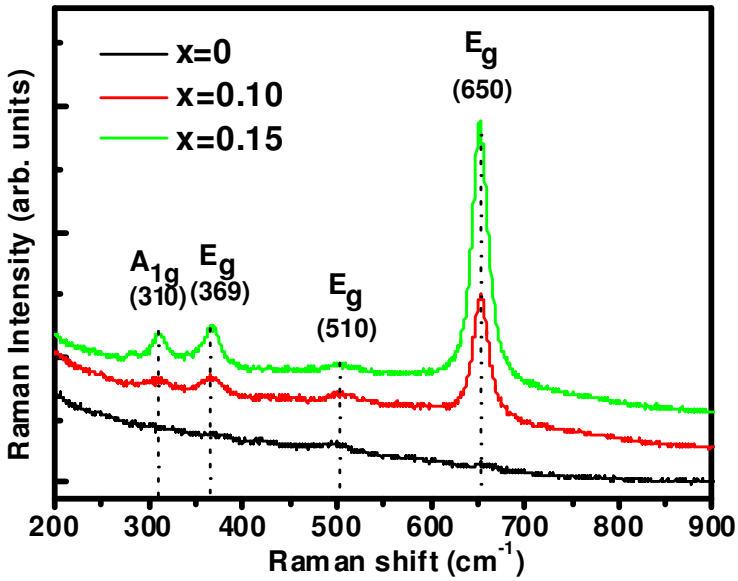

Fig. 5:

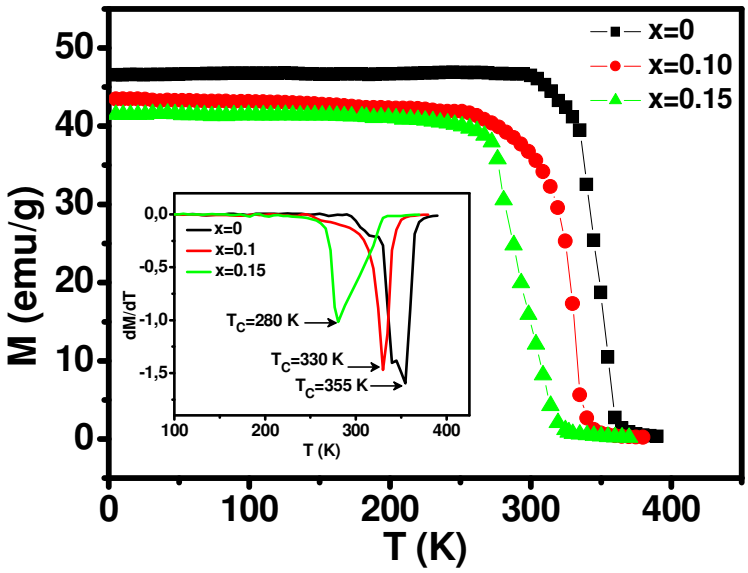

Fig.6:

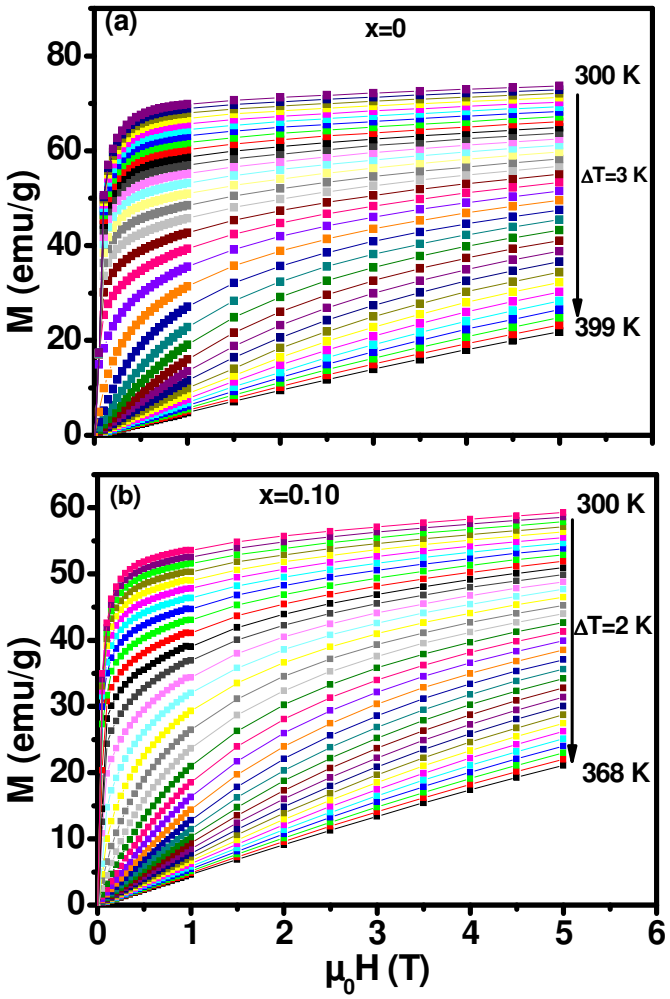

Fig.7:

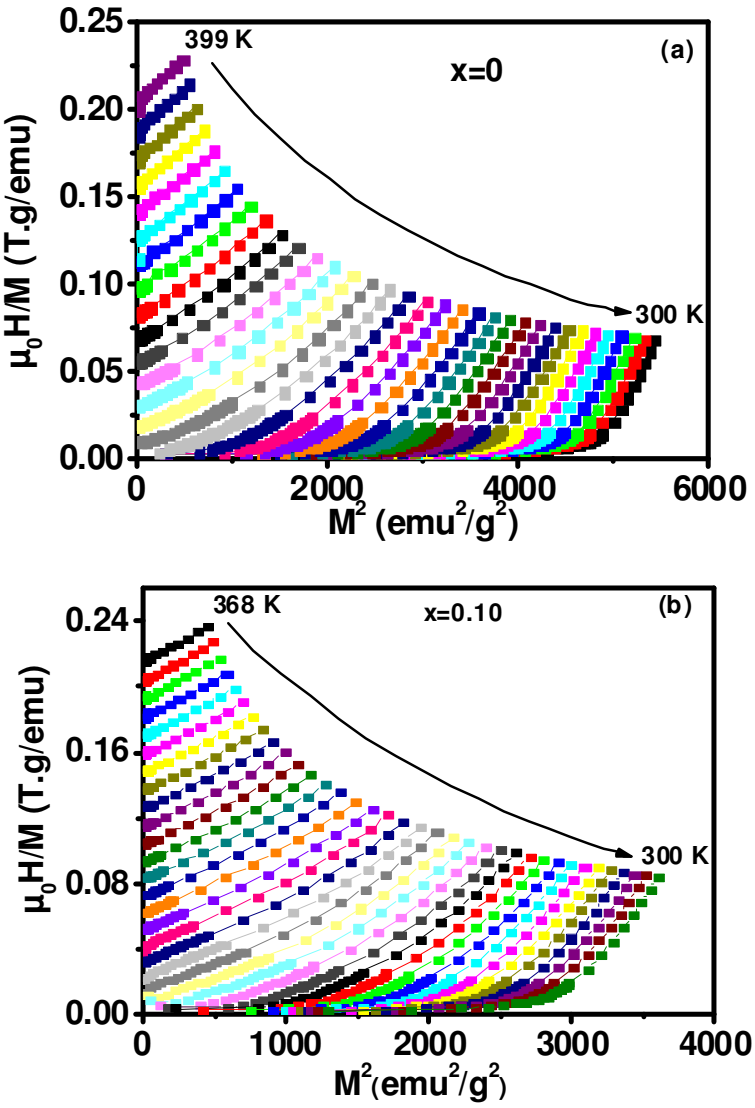

Fig.8:

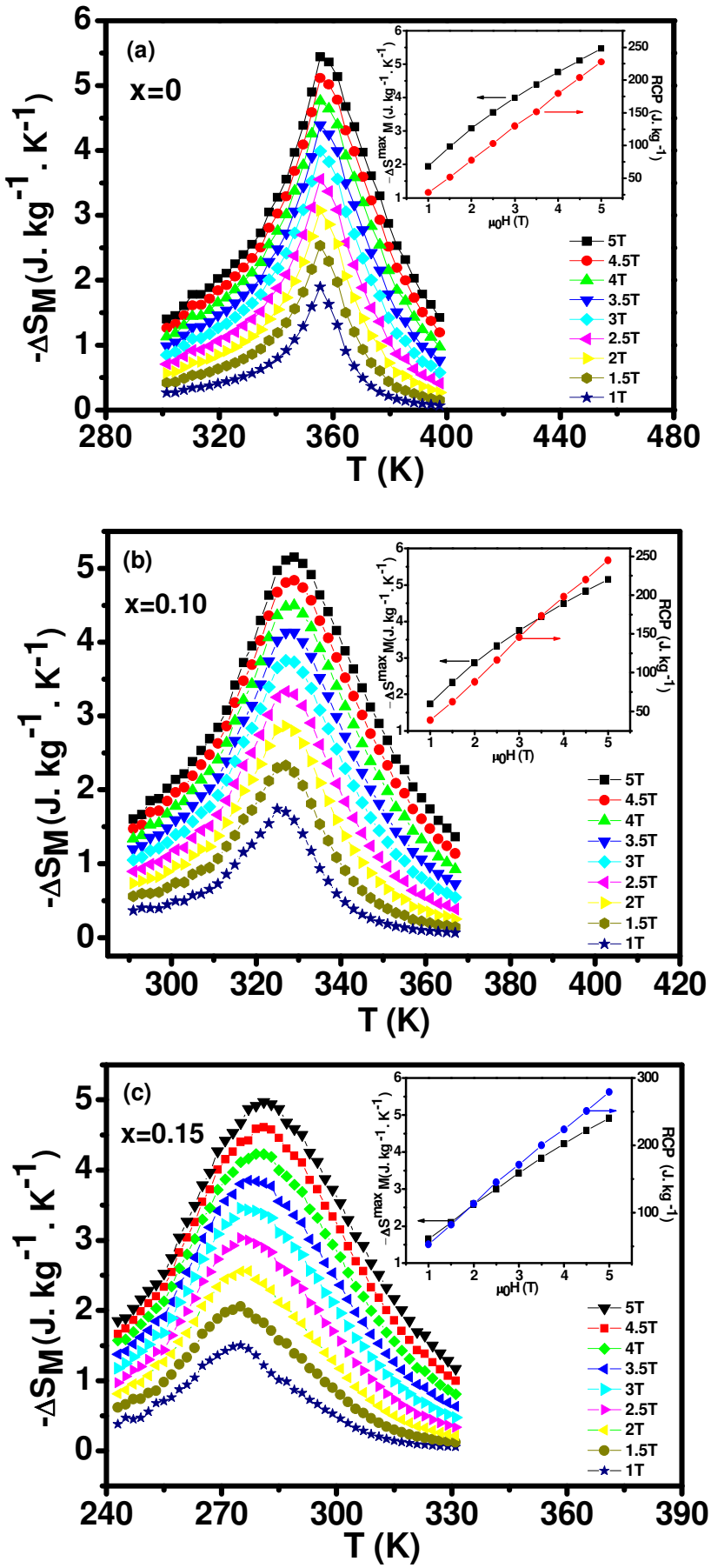

Fig.9:

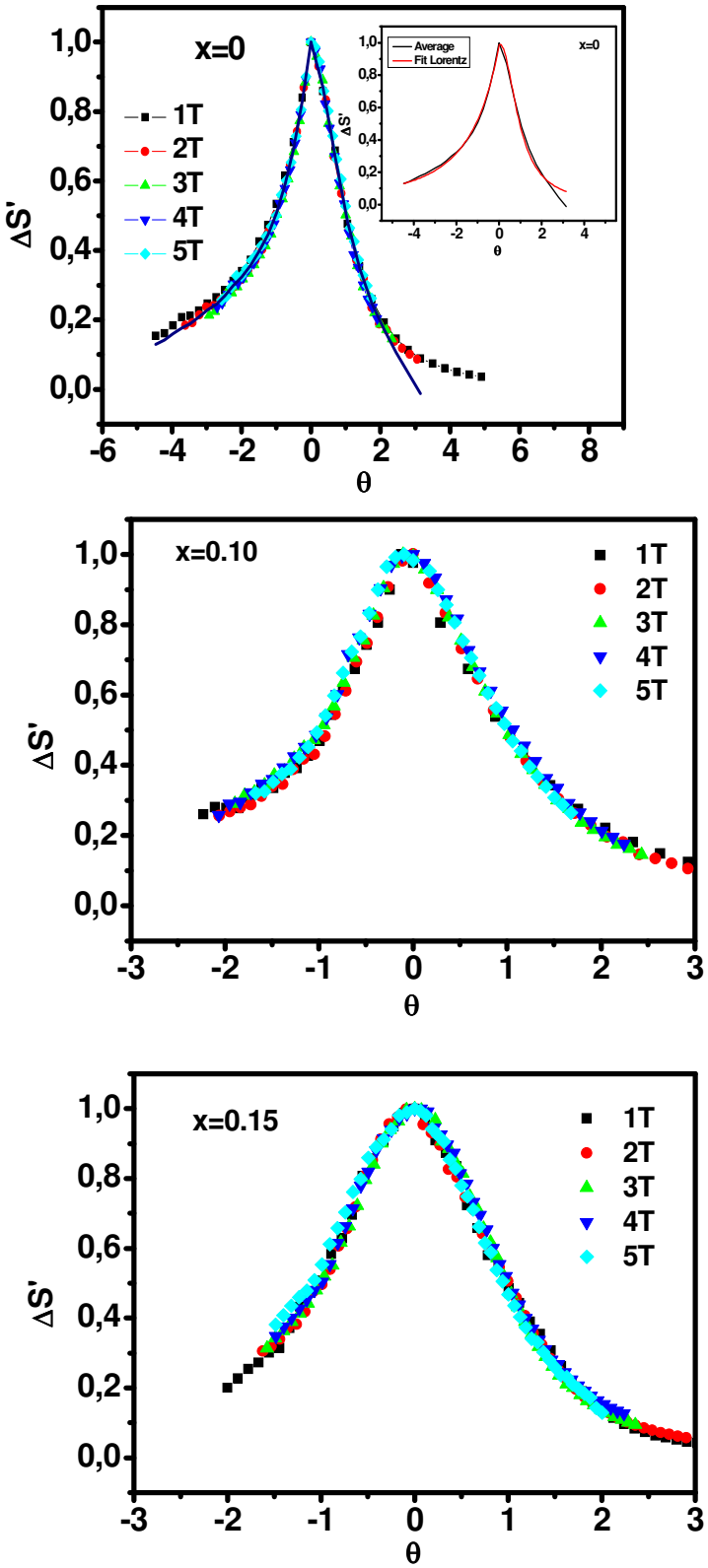

Fig.10:

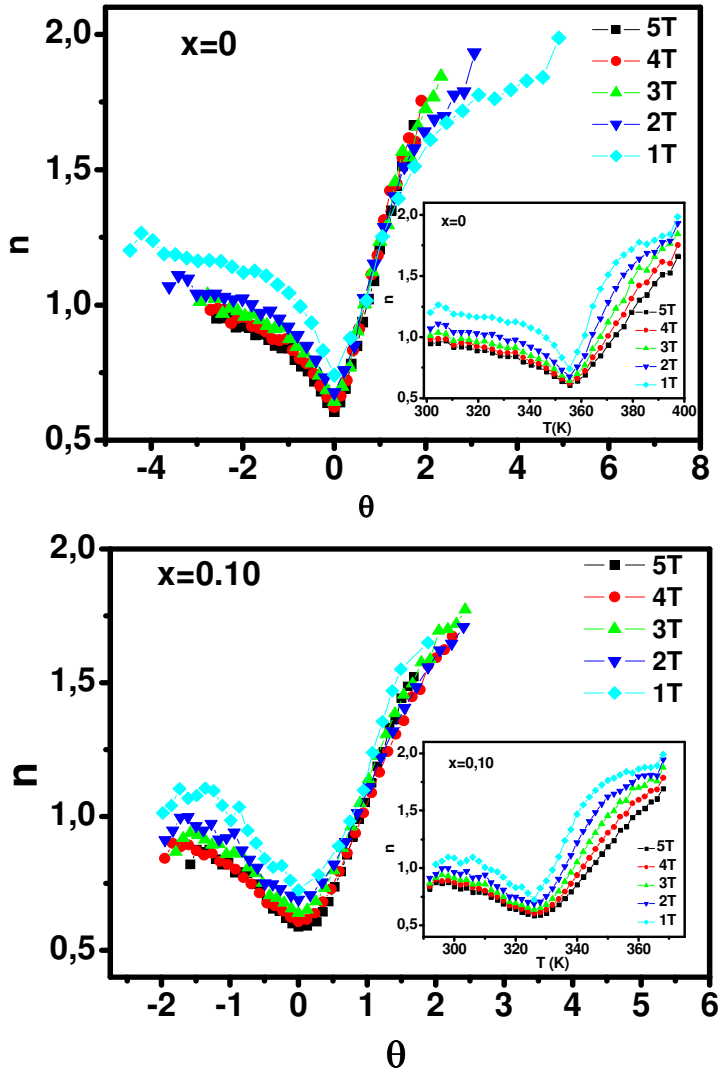

Table 1.

Sample	*0*	*0.10*	*0.15*
Structure type	*Rhombohedral*	*Rhombohedral*	*Rhombohedral*
Space group	*R-3c*	*R-3c*	*R-3c*
a (Å)	*5.5130 (2)*	*5.5135(3)*	*5.5266(2)*
c (Å)	*13.3833 (1)*	*13.3844 (2)*	*13.3927 (1)*
V ($Å^3$)	*352.263 (3)*	*352.785 (1)*	*352.997 (2)*
La/Eu/Sr B_{iso} ($Å^2$)	*0.55*	*0.79*	*0.82*
Mn B_{iso} ($Å^2$)	*0.86*	*0.84*	*0.51*
(O)B_{iso} ($Å^2$)	*1.22 (3)*	*1.20 (5)*	*1.19 (1)*
x (O)	*0.4785(3)*	*0.4544(3)*	*0.4473 (3)*
d_{Mn-O} (Å)	*1.952 (6)*	*1.958 (3)*	*1.961 (4)*
$\Theta_{(Mn-O-Mn)}$ (°)	*166.568 (7)*	*165.24 (6)*	*164.55 (2)*
R_{wp} (%)	*2.43*	*2.23*	*2.56*
R_p (%)	*1.78*	*1.69*	*2.63*
R_F (%)	*2.65*	*2.39*	*2.15*
χ^2 (%)	*1.89*	*1.93*	*1.74*
Band width W (arb. u.)	*0.09557*	*0.09441*	*0.09383*
Curie temperature T_C (K)	*355*	*330*	*280*
Tolerance factor t	*0.9266*	*0.8914*	*0.8787*
Grain size GS (nm)	*84*	*91*	*97*
Ratio Mn^{4+}/Mn^{3+}	*0.443*	*0.993*	*1.403*
Oxygen content y	*3.007*	*3.098*	*3.134*

Table 2.

Composition	*Typical cationic composition from EDX*				*Nominal composition*
	La	*Eu*	*Sr*	*Mn*	
x=0	*0.64(6)*	*0.05(3)*	*0.31(4)*	*1.06(2)*	$La_{0.65}Eu_{0.05}Sr_{0.30}MnO_3$
x=0.10	*0.63(8)*	*0.06(1)*	*0.21(2)*	*1.07(1)*	$La_{0.65}Eu_{0.05}Sr_{0.20}MnO_3$
x=0.15	*0.63(4)*	*0.06(1)*	*0.16(3)*	*1.09(1)*	$La_{0.65}Eu_{0.05}Sr_{0.15}MnO_3$

Table 3.

Composition	T_C (K)	ΔH (T)	$\lvert-\Delta S_M^{max}\rvert$ (J. kg^{-1}. K^{-1})	RCP (J. kg^{-1})	Ref.
Gd	*293*	1	*3.25*	-	36
$La_{0.665}Eu_{0.035}Sr_{0.3}MnO_3$	*357*	1	*1.58*	*42.3*	38
$La_{0.56}Eu_{0.14}Sr_{0.3}MnO_3$	*306*	1	*1.46*	*47.7*	38
$La_{0.65}Eu_{0.05}Sr_{0.3}MnO_3$	*355*	1	*1.89*	*33*	This work
$La_{0.65}Eu_{0.05}Sr_{0.2}MnO_3$	*330*	1	*1.74*	*42*	This work
$La_{0.65}Eu_{0.05}Sr_{0.15}MnO_3$	*280*	1	*1.5*	*54*	This work
$La_{0.67}Ba_{0.33}Mn_{0.98}Ti_{0.02}O_3$	*310*	1	*0.93*	*45*	18
Gd	*293*	5	*9.5*	*410*	37
$La_{0.65}Eu_{0.05}Sr_{0.3}MnO_3$	*355*	5	*5.44*	*230*	This work
$La_{0.65}Eu_{0.05}Sr_{0.2}MnO_3$	*330*	5	*5.15*	*245*	This work
$La_{0.65}Eu_{0.05}Sr_{0.15}MnO_3$	*280*	5	*4.96*	*283*	This work
$La_{0.65}Eu_{0.05}Sr_{0.3}Mn_{0.9}Cr_{0.1}O_3$	*310*	5	*3.35*	*207*	16
$La_{0.67}Ba_{0.33}Mn_{0.98}Ti_{0.02}O_3$	*310*	5	*3.19*	*307*	18
$La_{0.7}Sr_{0.3}Mn_{0.93}Fe_{0.07}O_3$	*296*	5	*4.0*	*225*	20